Research Square

Preprints are preliminary reports that have not undergone peer review.
They should not be considered conclusive, used to inform clinical practice,
or referenced by the media as validated information.

Strain engineering-induced photothermal enhancement: Co/MnO@C heterostructure for high-performance phase change materials

JiaJia Li
Shandong University of Technology
Qingyang Du
Shandong University of Technology
Hao Zheng
Shandong University of Technology
Wenjun Dong
University of Science and Technology
Cheng Dong
Shandong University of Technology
Ang Li
angli@usts.edu.cn

Shandong University of Technology

Research Article

Keywords: phase change materials, photothermal conversion, thermal energy storage, strain engineering, phonon-driven energy conversion

Posted Date: November 20th, 2026

DOI: https://doi.org/10.21203/rs.3.rs-10960014/v1

License: This work is licensed under a Creative Commons Attribution 4.0 International License.
Read Full License

Additional Declarations: No competing interests reported.

Abstract

Carbon-based photothermal phase change materials (PCMs) is one of the most effective photothermal storage materials which offer a promising route to convert intermittent solar energy into storable thermal energy, however face intrinsic limitations from uncontrollable carbon skeleton defects and poorly tunable non-radiative relaxation pathways. In this study, we propose a novel strain engineering induced photothermal enhancement strategy, in which a metal-organic framework (MOF)-on-MOF-derived heterostructure is constructed to design a Co/MnO@C porous framework for encapsulating PCMs. The lattice mismatch between Co and MnO introduces localized strain, inducing the formation of interfacial defect states. Interfacial defect states serve as non-radiative recombination centers, efficiently converting solar energy into lattice thermal energy. After PCMs encapsulation, the composite achieved a photothermal conversion efficiency of 96.3% with 100 mW/cm^2 solar irradiation. Photo-thermal-electric tests returned sustained outputs of 91.3 mV and 26.9 mA from the composite. It also achieves an improvement in formaldehyde removal in photocatalytic degradation and shows excellent anti-icing and de-icing capabilities. This work expands the application of strain engineering from charge control to phonon-driven energy conversion, offering a new idea for designing efficient and multi-functional photothermal storage materials.

1 Introduction

With global energy demand continuing to rise, developing renewable energy has become one of the key paths to achieving sustainable development[1, 2]. However, renewable energy, like solar power, is highly intermittent and unstable, which leads to a serious mismatch between energy supply and demand across time and space, greatly limiting its large-scale grid integration and efficient use[3]. Phase change materials (PCMs) can store a large amount of latent heat at nearly constant temperatures, making them ideal for buffering the fluctuations in solar energy supply and regulating the time difference between energy supply and demand through heat storage and release, thus achieving smooth thermal management[4, 5]. However, traditional PCMs have weak solar radiation absorption and low photothermal conversion efficiency, severely limiting their feasibility as standalone materials in solar thermal collection systems[6, 7].

When carbon-based nanomaterials (e.g., graphene, carbon nanotubes) are incorporated into a phase change matrix, the spectral response of the composite shifts toward the solar radiation band. However, traditional carbon nanofillers are prone to agglomeration, and their intrinsically fixed pore structures are difficult to control[8, 9]. Metal-organic framework (MOF)-derived carbons inherit the pore geometry of their parent frameworks, which yields carbon networks that carry large surface areas and tiered porosity[10, 11]. Metal nanoparticles such as Fe, Co, and Ni embedded in these carbon scaffolds harvest photons across a wider spectrum via localized surface plasmon resonance (LSPR)[12]. The non-radiative relaxation of photogenerated carriers in MOF-derived carbon materials is still limited by structural

defects like the disordered channels and metal particle agglomeration formed in the carbon framework during high-temperature pyrolysis[13].

To tackle this challenge, heterostructured carbon materials built using the MOF-on-MOF strategy show unique advantages[14, 15]. By choosing two MOFs with different lattice constants as precursors, a controllable lattice mismatch is introduced at their epitaxial growth interface, which then produces local strain fields in the composite carbon framework after carbonization[16, 17]. This strain can induce defect states at the interface, such as oxygen vacancies and carbon framework defects, which act as efficient non-radiative recombination centers capable of trapping photogenerated carriers[18]. The trapped carriers then transfer energy step by step to the surrounding lattice through multiphonon emission, achieving robust electron-phonon coupling and efficiently converting light energy into lattice heat[19, 20]. Strain engineering offers a fresh way to control the carrier relaxation dynamics in photothermal conversion.

The strategy of introducing local strain through lattice mismatch has been studied in fields such as electrocatalysis[21, 22], thermoelectric conversion[23, 24], and semiconductor light-emitting devices[25]. In electrocatalysis, lattice strain tuned the d-band center position by modulating atomic spacing and orbital interactions, thereby altering the adsorption energy of reaction intermediates[26, 27]. This optimized the catalytic activity for key electrochemical processes such as the hydrogen evolution reaction (HER), oxygen evolution reaction (OER), and CO_2 reduction reaction (CO_2 RR). Lattice distortion was also found to effectively regulate carrier migration kinetics, tune surface chemistry, and enhance catalytic stability[28, 29]. In thermoelectric research, engineered lattice strain effectively reduced lattice thermal conductivity by broadening phonon dispersion[30, 31]. In semiconductor light-emitting devices, lattice strain precisely guided efficient radiative recombination of carriers through refined band engineering, leading to semiconductor light-emitting devices with controllable wavelength, outstanding efficiency, and prolonged lifetime[32, 33]. In these fields, strain is typically employed to promote charge separation, suppress phonon transport, or facilitate radiative recombination. However, for photothermal applications, photogenerated charge carriers are required to undergo non-radiative relaxation processes, through which energy is transferred to the crystal lattice via electron-phonon coupling and subsequently released as heat. Therefore, a rational structural design is required and unsolved to realize directional enhancement of non-radiative relaxation channels via strain engineering.

This study proposes a photothermal enhancement strategy induced by lattice strain engineering. MOF (Mn) is grown on the surface of ZIF-67, and Co/MnO@C structure is obtained through high-temperature carbonization. The lattice mismatch between Co and MnO generates localized lattice strain and thereby promotes interfacial defect states such as carbon defects and oxygen vacancies. These interfacial defect states that form at the Co/MnO@C interface act as non-radiative recombination centers where captured electrons dissipate energy through lattice vibrations. After encapsulation with polyethylene glycol (PEG), the composite reached a photothermal conversion efficiency of 96.3% under 100 mW/cm^2 irradiation. When PEG-Co/MnO@C was used as the photothermal layer in a photothermal-electric device,

and it generated 91.3 mV and 26.9 mA under the same conditions. The same material proved effective for photocatalytic formaldehyde degradation. When further employed to encapsulate paraffin wax (PW), it enabled the fabrication of hydrophobic surfaces that offer robust anti-icing/de-icing functionality. This work extends lattice strain engineering from charge modulation to phonon regulation, a transition that points toward improved photothermal converters and multifunctional energy storage materials.

2 Experimental

2.1 Materials

The following reagents were used as received. $Co(NO_3)_2$ $6H_2O$, triethylamine, DMF, methanol, and ethanol came from Tianjin Zhiyuan Chemical Reagent Co., Ltd. $MnCl_2$ $4H_2O$, 2-methylimidazole, and 2-aminoterephthalic acid were sourced from Shanghai Macklin Biochemical Technology Co., Ltd. Aladdin Biochemical Technology Co., Ltd. supplied PEG (Mn = 10000 g/mol), while PW (C18-C30) was provided by Hebei Hongzhuangyuan Co., Ltd. The PTFE emulsion (60 wt% solids) was purchased from dodochem.com.

2.2 Preparation of ZIF-67@MOF(Mn)

A typical synthesis procedure was carried out as follows. ZIF-67 (150 mg) was dissolved in DMF (50 mL). $MnCl_2{\cdot}4H_2O$ (2 mmol) was subsequently added to the above solution, and the resulting mixture was magnetically stirred for 12 h. 2-Aminoterephthalic acid (1 mmol) was then introduced. After complete dissolution, triethylamine (1 mmol) was added dropwise to the mixture, and the reaction was allowed to proceed for 120 min under continuous stirring. The as-obtained precipitate was separated by centrifugation, rinsed successively with DMF and methanol (three times each), and finally dried.

2.3 Preparation of supporting materials

Thermal treatment of ZIF-67, MOF(Mn), and ZIF-67@MOF(Mn) was carried out at 800°C under argon for 5 h. The carbonized products were collected as black powders and labeled Co@C, MnO@C, and Co/MnO@C, respectively.

2.4 Synthesis of composite PCMs

Composite PCMs were prepared by melt blending. The supporting materials were dried at 80 ℃ for 12 h under vacuum. Dried supports and PEG were then mixed at a predetermined mass ratio in a mortar and ground thoroughly at room temperature. The mixture was heated at 80 ℃ to melt PEG completely, cooled, and ground again. This melting-cooling-grinding cycle was repeated to ensure uniform PEG loading. Finally, the product was dried in a vacuum oven at 80 ℃ for 24 h.

3 Results and discussion

Figure 1a illustrates the schematic synthesis process of PEG-Co/MnO@C. First, ZIF-67 precursors with a dodecahedral morphology were prepared through a coordination reaction, followed by the growth of a manganese-based MOF on the surface of ZIF-67. During the subsequent high-temperature carbonization, the Co/MnO@C with abundant oxygen vacancies and carbon defects was obtained. PEG was then impregnated into the Co/MnO@C to yield the photothermal composite PCMs. XRD (**Fig. S1a**) and FT-IR (**Fig. S1b**) showed good agreement, with the characteristic peaks of ZIF-67@MOF(Mn) matching those of ZIF-67 and MOF(Mn), thus confirming the successful growth of MOF(Mn) on ZIF-67[34]. SEM images demonstrated ZIF-67 to exhibit a typical dodecahedral morphology with a smooth and dense surface (**Fig. S2a)**. Upon the growth of MOF(Mn) (**Fig. S2b**), the surface of ZIF-67@MOF(Mn) became rough (**Fig. S2c**). Upon carbonization, the basic morphological structure of ZIF-67 remained intact, although its size decreased slightly due to the carbonization of organic ligands (**Fig. S2d**)[35]. Following the formation of the Co/MnO@C, spherical particles covered the surface of the material (**Fig. S2e and f**).

The XRD results (Fig. 1b) confirmed that Co/MnO@C was composed of metallic Co and MnO phases. Specifically, metallic Co existed in Co@C, showing a distinct and intense sharp peak at 44.2°, assigned to the (111) crystal plane of Co. MnO existed in MnO@C, showing a prominent peak at 40.6°, assigned to the (200) crystal plane of MnO. Furthermore, compared with Co@C, the diffraction peak of the Co (111) plane in Co/MnO@C shifted to a lower angle by 0.11°. Compared with MnO@C, the diffraction peak of the MnO (200) plane in Co/MnO@C shifted to a lower angle by 0.03° (Fig. 1c)[36]. These results indicated that after Co/MnO@C formed, lattice strain may have occurred in both Co and MnO.

TEM analysis was conducted to further reveal the precise structural features of Co/MnO@C. The results showed that the two types of nanoparticles were closely packed, thereby forming a heterointerface (Fig. 1d). HRTEM images revealed the lattice strain of Co and MnO. The interplanar spacing of the Co (111) plane in Co/MnO@C was measured to be 0.21 nm, compared with 0.205 nm for Co, corresponding to a tensile lattice strain of approximately 2.4% (Fig. 1e)[37]. In addition, some lattice fringes of Co/MnO@C with lattice strain exhibited a disordered distribution, leading to the formation of high-density lattice distortions and local strain (Fig. 1f)[38]. The lattice strain between Co and MnO could regulate the band structure, photogenerated carrier mobility and oxygen vacancy formation, which showed great potential in improving the photothermal conversion performance of the material[39]. The HAADF image and corresponding EDS elemental mappings (Fig. 1g) of Co/MnO@C revealed that the spatial distributions of Mn and O coincided, while Co was primarily located at the periphery of these regions, further confirming the formation of the Co/MnO heterointerface.

FT-IR spectroscopy was employed to analyze the chemical bonding features of Co@C, MnO@C, and Co/MnO@C (Fig. 2a). For all samples, the 1562 cm^{-1} peak corresponded to the asymmetric and symmetric stretching of the C = C bonds in the benzene ring[40]. The peak at 471 cm^{-1} for MnO@C was assignable to the stretching mode of the Mn-O bond in MnO[41]. In contrast, Co/MnO@C showed a red shifted Mn-O peak at 464 cm^{-1}, revealing a longer Mn-O bond than MnO@C[42]. In addition, the C-O peak for Co/MnO@C at 1103 cm^{-1} was shifted with respect to those for Co@C and MnO@C, revealing a

longer C-O bond[43]. These bond distortions were presumably caused by the lattice strain between Co and MnO, which induced bond elongation[44].

Raman spectra showed the presence of both D and G peaks in all samples. (Fig. 2b). The 1350 cm^{-1} D-band signified carbon disorder, whereas the 1590 cm^{-1} G-band arose from sp^2 graphitized carbon. The I_D/I_G ratio was used to characterize the defect degree of the carbon materials. Specifically, Co@C, MnO@C, and Co/MnO@C exhibited I_D/I_G values of 0.80, 0.82, and 1.05, respectively. The highest defect degree of Co/MnO@C suggested that lattice strain between Co and MnO distorted the carbon skeleton. The abundant defect sites facilitated non-radiative relaxation of photogenerated carriers and enhance electron-phonon coupling[45, 46]. Furthermore, Co@C showed a characteristic Co-Co peak at 664 cm^{-1}, whereas MnO@C displayed a Mn-O peak at 644 cm^{-1}[47, 48]. Notably, in Co/MnO@C, the Mn-O vibrational peak shifted to 633 cm^{-1}, suggesting that the lattice strain between Co and MnO altered the bond length of the Mn-O bond, which was consistent with the FT-IR results[49]. DFT calculations (Fig. 2c **and Fig. S3**) were carried out for the construction of surface models of the MnO (200) plane in MnO@C and Co/MnO@C. The calculated Mn-O bond lengths were 2.22 Å for MnO@C and 2.28 Å for Co/MnO@C, further confirming that lattice strain modulated the Mn-O bond length.

The XPS survey spectra (**Fig. S4a**) confirmed the coexistence of C, N, and O in all three samples, with additional Co in Co@C and Co/MnO@C, and Mn in MnO@C and Co/MnO@C. Three peaks at 284.80, 285.75, and 290.55 eV were resolved from the C 1s spectra of all samples, corresponding to C-C/C = C, C-N, and C = O species, respectively (**Fig. S4b**)[50]. The N 1s spectra of all samples were fitted to oxidized N, graphitic N, and pyridinic N species (**Fig. S4c**)[51]. The Co 2p spectra of Co@C and Co/MnO@C revealed peaks corresponding to Co^0, Co^{2+}, Co^{3+}, and satellite features (Fig. 2d). Compared with the Co^0 peak of Co@C located at 778.82 eV, the corresponding peak of Co/MnO@C was shifted to a lower binding energy of 778.50 eV[52]. Meanwhile, the Mn 2p spectra of MnO@C and Co/MnO@C were fitted to Mn $2p_{3/2}$, Mn $2p_{1/2}$, and their satellite peaks (Fig. 2e). In contrast to the Mn $2p_{3/2}$ peak of MnO@C at 641.61 eV, the corresponding peak of Co/MnO@C was shifted to a higher binding energy of 641.67 eV[53]. The above binding energy shifts are attributable to lattice strain at the Co/MnO heterointerface, which alters interatomic distances and the electron cloud distribution[54]. Deconvolution of the O 1s spectrum for Co/MnO@C yielded peaks at 530.04, 531.89, and 533.74 eV, corresponding to M-O bonds, oxygen vacancies, and C-O bonds, respectively (Fig. 2f)[55, 56]. Since lattice strain reduced the oxygen vacancy formation energy, the oxygen vacancy concentration in Co/MnO@C was higher than that in both Co@C and MnO@C (**Tab. S1**)[57].

DFT calculations yielded work functions of 5.14 eV for Co (111) and 2.90 eV for MnO (200) (Fig. 2g). Because MnO (200) had a lower work function than Co (111), its Fermi level was suggested to sit higher[58, 59]. When the two phases came into contact, electrons were driven from MnO to Co, a direction that was consistent with the binding energy shifts in the XPS spectra. MnO was left positively charged while Co accumulated negative charge, and this interfacial charge separation triggered band bending

that eventually pulled the Fermi levels into alignment (Fig. 2h). PDOS data (Fig. 2i) placed the Co (111) d-band center at -1.89 eV for Co@C and at -2.07 eV for Co/MnO@C. This 0.18 eV shift downward stems from strain at the Co/MnO interface[60]. DFT charge density difference plots (Fig. 2j) further revealed the redistribution of electrons, with the MnO side losing charge (blue) and the Co side gaining it (red) This result directly demonstrated that electrons tended to transfer from MnO to Co, leading to pronounced charge enrichment around the Co site.

The pore structure characteristics were characterized by N_2 adsorption-desorption measurements (**Fig. S5**). All three samples displayed type IV isotherms with hysteresis loops, indicating the coexistence of micropores and mesopores.The pore volumes were 0.24 cm^3/g for Co@C, 0.19 cm^3/g for MnO@C, and 0.31 cm^3/g for Co/MnO@C (**Tab. S2**). Co/MnO@C showed a larger pore volume likely from gas evolution during carbonization due to Co/MnO interaction[61, 62]. The abundant pore volume enhanced the adsorption capacity of Co/MnO@C, thereby improving its energy storage density.

PEG molecules were impregnated into the Co/MnO@C to prepare the PEG-Co/MnO@C. The corresponding SEM images (**Fig. S6**) revealed that the surface roughness of PEG-Co/MnO@C was significantly reduced, indicating that PEG was successfully filled into the porous structure of Co/MnO@C. XRD (**Fig. S7a**) and FT-IR (**Fig. S7b**) confirmed that PEG retained its characteristic diffraction peaks and functional groups in PEG-Co/MnO@C, indicating physical combination with no chemical reaction between PEG and Co/MnO@C.

DSC was used to characterize the thermal behavior of PEG-Co/MnO@C. Figure 3a, b **and Tab. S3** listed the enthalpies and phase transition temperatures of PEG and the composite PCMs. Melting and crystallization gave distinct endothermic and exothermic peaks for all samples, marking the solid-liquid and liquid-solid phase transitions of PEG. The crystallinities were 86.9% (PEG-Co@C), 89.0% (PEG-MnO@C), and 91.6% (PEG-Co/MnO@C). Among them, PEG-Co/MnO@C exhibited the highest crystallinity, which was ascribed to the weakest confinement effect exerted by the Co/MnO@C on the PEG chains, thereby facilitating their chain ordering and crystallization. In addition, Co/MnO@C possessed an appropriate pore size and the largest pore volume, which provided sufficient physical space for the accommodation of PEG molecular chains. Consequently, PEG-Co/MnO@C demonstrated the highest melting and solidification enthalpies (Fig. 3c). These results indicated that PEG-Co/MnO@C, with a certain latent heat storage capacity, can meet the requirements for thermal energy storage and release.

The non-isothermal phase change kinetics of PEG and PEG-Co/MnO@C were examined by DSC. Both samples showed endotherms and exotherms in their DSC curves (**Fig. S8**). **Tab. S4** summarized T_p and $t_{1/2}$ values at various cooling rates. The composite consistently gave shorter $t_{1/2}$ than PEG, suggesting that the porous structure promoted nucleation. The temperature and time dependence of the relative crystallinity (Fr) was then examined for PEG and PEG-Co/MnO@C. The Fr-T (Fig. 3d, e) and Fr-t curves **(Fig. S9**) showed that faster cooling lowered the peak temperature and shortened the half-crystallization time. Furthermore, both PEG and PEG-Co/MnO@C exhibited excellent linear relationships in their lnΦ-lnt

curves (Fig. 3f, g). **Tab. S5** showed that F(T) rose with relative crystallinity, and higher F(T) corresponded to slower crystallization. Notably, PEG-Co/MnO@C had a lower F(T) than PEG, meaning the composite shortened the nucleation time of PEG molecules. The Kissinger method gave the apparent activation energy for the non-isothermal phase transition (Fig. 3h, i). PEG-Co/MnO@C had a value of -8.24 $kJ \cdot mol^{-1}$, compared with − 4.34 $kJ \cdot mol^{-1}$ for PEG. The lower value for the composite meant a narrower heat-release temperature range and a faster thermal response.

TGA (**Fig. S10**) was employed to evaluate the thermal stability of the materials. Co/MnO@C exhibited negligible decomposition up to 800°C. PEG-Co/MnO@C remained stable below 240°C. This temperature covered the phase transition point of PEG, indicating its applicability in this regime. After 300 thermal cycles, the DSC curves of PEG-Co/MnO@C showed no significant changes (**Fig. S11**), confirming its cycling stability. The composite also maintained its structural integrity over the same period (**Fig. S12**).

UV-Vis-NIR spectra presented in **Fig. 4a** were recorded for evaluating the light absorption properties of the examined materials. PEG exhibited only weak absorbance across the entire measured wavelength range. For Co@C, the carbon component contributed to a broadband absorption covering the full spectrum, whereas the localized surface plasmon resonance of Co nanoparticles additionally strengthened the response in the UV-vis region. In the case of MnO@C, the observed absorption stemmed jointly from the intrinsic band transitions of MnO and from defect levels introduced by oxygen vacancies[63]. These two mechanisms offered extra channels for electron excitation, thereby effectively enhancing the absorbance of MnO@C. The heterostructure between Co and MnO in Co/MnO@C created lattice strain, which in turn caused distortion. The distortion altered the electron cloud and produced defect states at the interface, providing more transition channels for electrons. As a result, the absorption extended from visible to near infrared, covering the full spectrum[64]. Hence, even after loading with PEG, the composite PCMs retained their excellent light absorption characteristics.

Time-temperature profiles were obtained under simulated solar irradiation (**Fig. 4b**). With 100 mW/cm^2 solar irradiation, PEG showed a gradual temperature increase to ~ 51.5°C, consistent with its weak light absorption. However, the composite PCMs showed a rapid temperature rise that subsequentiy reached a phase change plateau, corresponding to the melting endotherm of PEG. Upon removal of the solar irradiation, the composite PCMs dropped rapidly, accompanied by another plateau associated with the crystallization exothermic process of PEG. Maximum temperatures for PEG-Co@C, PEG-MnO@C, and PEG-Co/MnO@C reached approximately, 84.0°C, 80.9°C and 88.7°C **(Fig. 4c**), with corresponding photothermal conversion efficiencies were determined to be 86.9%, 90.7% and 96.3%, respectively (**Fig. 4d**). These results indicated that the lattice strain between Co and MnO generated interfacial defect states, where photogenerated electrons, instead of recombining, were trapped by these defect states and released energy as heat via non-radiative relaxation pathways. The heat-transfer characteristics were further investigated by infrared thermal imaging (**Fig. 4e**). Compared with PEG, PEG-Co/MnO@C exhibited a faster temperature-rise rate, reflecting its superior photothermal conversion capability. Furthermore, after 10 consecutive cycles (**Fig. 4f**), no significant change was observed in the

temperature-time profiles of PEG-Co/MnO@C, confirming the outstanding cycling stability of the material. The lattice strain engineering strategy overcame the limitation of the single photothermal mechanism in conventional carbon-based materials, achieved synergistic enhancement among multiple components, and significantly improved the photothermal conversion performance, surpassing many values reported in the existing literature (**Fig. 4g**).

The photothermal enhancement mechanism of PEG-Co/MnO@C was illustrated in **Fig. 4h**. Photothermal enhancement of Co/MnO@C heterostructure originated from the localized strain field induced by interfacial lattice mismatch and its modulation of carrier relaxation pathways. The LSPR effect of Co nanoparticles produced strong absorption from visible to NIR, whereas MnO offered additional UV-vis absorption through interband transitions. Meanwhile, interfacial defect states induced by lattice strain introduced intermediate energy levels within the bandgap of MnO, providing additional transition channels for low energy photons. The synergistic effect of these three components enabled efficient solar full-spectrum solar harvesting. Upon photoexcitation, the built in electric field at the Co/MnO heterointerface drove the photogenerated carriers to migrate toward the MnO side. Once transferred to the MnO bulk, these carriers were trapped by strain-induced defect states, whereupon they released energy to the lattice in the form of heat through non-radiative relaxation pathways. The carbon framework served as an efficient thermal conduction network. It rapidly conducted the lattice heat from the interfacial defect sites of the Co/MnO@C heterostructure to the encapsulated PEG. This process drove the solid-liquid phase transition of PEG and accomplished thermal energy storage and release.

.

Figure 4 (a) UV-Vis-NIR absorption spectra of Co@C, MnO@C, Co/MnO@C, PEG-Co/MnO@C, PEG. (b) Time-temperature evolution curves, (c) saturation temperature and (d) corresponding photothermal storage efficiencies of PEG-Co@C, PEG-MnO@C, PEG-Co/MnO@C and PEG under solar simulator radiation at an intensity of 100 mW/cm^2. (e) Infrared thermal images of PEG and PEG-Co/MnO@C. (f) Time-temperature evolution curves of PEG-Co/MnO@C during photothermal cycling. (g) Comparison of photothermal performance of PEG-Co/MnO@C with that of the composite PCMs reported in the literature.

PEG-Co/MnO@C also exhibited potential photo-thermal-electric energy conversion and photocatalytic formaldehyde removal performance, providing a new strategy for the synergistic integration of power generation and formaldehyde degradation in environmentally friendly indoor environments (Fig. 5a). After placing PEG-Co/MnO@C on the hot side of the thermoelectric chip with the cold side immersed in an ice-water bath, it was integrated with a commercial thermoelectric module, enabling continuous output of stable voltage and current based on the Seebeck effect[65]. The photo-thermal-electric conversion performance of PEG and PEG-Co/MnO@C was measured at 100, 150, and 200 mW/cm^2. At light intensities of 100, 150, and 200 mW/cm^2, the output voltage of PEG-Co/MnO@C was 91.3 mV, 160.0 mV, and 195.0 mV, respectively (Fig. 5b, c), and the output current was 26.9 mA, 33.8 mA, and 52.8 mA, respectively (Fig. 5d, e). The composite thus delivered stable voltage and current generation,

substantially outperforming PEG. The photo-thermal-electric system was used to charge a mobile phone, drive an electric fan, and power a light bulb under 200 mW/cm^2 solar irradiation (Fig. 5f). Output power densities of PEG-Co/MnO@C at 100, 150, and 200 mW/cm^2 were 1.5, 3.3, and 6.4 W/m^2, respectively (Fig. 5g **and Tab. S6**). This power output is sufficient for small electronics, suggesting the viability of this system for low power portable devices[66]. Moreover, after 10 cycles, no significant change in voltage was observed, confirming the excellent cycling stability of this material for photo-thermal-electric energy conversion applications (Fig. 5h).

PEG-Co/MnO@C exhibited a certain photocatalytic formaldehyde removal performance (Fig. 5i). With 100 mW/cm^2 solar irradiation, the formaldehyde removal rate was 36.4% higher than that in the absence of light, confirming the feasibility of photothermal catalytic degradation of formaldehyde (Fig. 5j). Kinetic modeling was performed to evaluate the adsorption behavior of PEG-Co/MnO@C (**Table S7**)[67]. Both pseudo-first-order and pseudo-second-order kinetic models gave R^2 values close to unity, indicating that the adsorption of HCHO onto PEG-Co/MnO@C was not a simple physical adsorption process but rather a synergistic result of combined physical and chemical adsorption.

Co/MnO@C offered a new strategy for anti-icing/de-icing applications (Fig. 6a). To achieve a hydrophobic surface, PW was encapsulated into Co/MnO@C, and its performance was compared with that of natural wood. (Fig. 6b). Continuous droplet impact tests showed that the roof surface with PW-Co/MnO@C resisted ice formation effectively. By contrast, water droplets on the bare wood surface stuck and froze heavily within the same period. This was attributed to the hydrophobic nature of the PW-Co/MnO@C surface, which prevented droplet condensation. PW-Co/MnO@C and PEG-Co/MnO@C showed contact angles of 106.2° and 56.4°, respectively (Fig. 6c). Owing to the hydrophobicity of the PW-Co/MnO@C surface, water droplets could slide off on an inclined surface with a tilt angle of 20° (Fig. 6d). In contrast, PEG-Co/MnO@C was hydrophilic, making droplet sliding difficult (**Fig. S13**).

Freezing of water droplets on PW-Co/MnO@C and wood was compared under low temperature (-20°C) and 100 mW/cm^2 (Fig. 6e), and the corresponding infrared thermal images were presented in Fig. 6f. Water droplets on the wood surface began to freeze at 112 s and were completely frozen at 246 s. In comparison, owing to its excellent photothermal conversion performance, water droplets on PW-Co/MnO@C remained unfrozen for more than 246 s and did not freeze even by 640 s, indicating that PW-Co/MnO@C possessed superior anti-icing performance under solar irradiation. PW-Co/MnO@C also exhibited de-icing performance. The melting process of ice on PW-Co/MnO@C and wood surfaces was compared under low temperature (-20°C) with 100 mW/cm^2 solar irradiation (**Fig. S14 and Fig. S15**). Ice on PW-Co/MnO@C began to melt at 120 s and was completely melted at 606 s, whereas no melting phenomenon was observed on the wood surface within 606 s. To further evaluate the de-icing performance of the hydrophobic PW-Co/MnO@C, a 4 mm thick ice film was prepared on both PW-Co/MnO@C and wood surfaces at -20°C, and the samples were then placed under a solar irradiance of 100 mW/cm^2. The ice film on PW-Co/MnO@C slid off after approximately 16 min, and the coating

surface temperature rose to nearly room temperature. In contrast, no ice sliding was observed on the wood surface within 16 min (Fig. 6g **and Fig. S 16**).

4. Conclusion

This work demonstrates a strain engineering-induced photothermal enhancement strategy by constructing a MOF-on-MOF-derived Co/MnO@C heterostructure for encapsulating PEG, achieving a synergistic combination of high photothermal conversion efficiency and multifunctional applicability. Comprehensive experimental and DFT computational analyses reveal that the lattice mismatch at the Co/MnO heterointerface induces significant interfacial strain, which modulates the electronic structure, promotes the formation of carbon defects and oxygen vacancies, and, together with the built-in electric field arising from the work function difference, effectively suppresses radiative charge recombination while facilitating non-radiative relaxation pathways for efficient photothermal conversion. With 100 mW/cm^2 solar irradiation, the photothermal conversion efficiency of PEG-Co/MnO@C reaches 96.3%. This material not only maintains stable voltage and current output but also increases the formaldehyde removal rate by 36.4% under solar irradiation. After encapsulating PW, PW-Co/MnO@C exhibits surface hydrophobicity capable of enabling anti-icing and de-icing functions. This study opens up new avenues for the development of durable, environmentally friendly, and highly efficient solar thermal energy storage systems, breaking through the limitations of single-mechanism constraints that have hindered carbon-based photothermal materials.

Declarations

Declaration of Competing Interest

The authors declare that they have no known competing financial interests or personal relationships that could have appeared to influence the work reported in this paper.

Supporting Information

Supplementary data associated with this article can be found in the online version.

Author Contribution

Jiajia Li: Data curation, Formal analysis, Writing - original draft. Qingyang Du: Writing - review & editing, Funding acquisition. Hao Zheng: Data curation, Formal analysis. Wenjun Dong: Formal analysis, Writing - review & editing. Cheng Dong: Formal analysis, Funding acquisition, Supervision, Writing - review & editing. Ang Li: Conceptualization, Formal analysis, Funding acquisition, Supervision, Writing - review & editing.

Acknowledgements

The work was supported by the National Natural Science Foundation of China (No. 52402297, 52672272), Natural Science Foundation of Shandong Province (ZR2026ZD27) and Key R&D Program of Shandong Province (2024CXGC010320, 2025TSGCCZZB0828). The authors would like to thank Shiyanjia Lab (www.shiyanjia.com) for the supports of TEM test.

Data availability

The authors are unable or have chosen not to specify which data has been used.

References

1. Su C, Shao L, Chen Z, Yang Y, Cui M, Zhang G, Ma J, Ji Z (2026) Ammonium polyphosphate@ZIF flexible polyurethane foam designed by the interface hydrogen bond network connection for thermal insulation and fire retardancy. Adv Compos Hybrid Mater 9:332. https://doi.org/10.1007/s42114-026-01890-9
2. Zhang S, Wang C, Guo Z (2025) Batteries for Grid-Scale Energy Storage Applications. Adv Mater 37:e16590. https://doi.org/https://doi.org/10.1002/adma.202516590
3. Liu Y, Cao X, Yang M, Wei M, Mao J, Sun J, Xiang H, Wang H (2025) Flame-retardant wood-based composite phase change materials based on polydopamine functionalized carbon dots for efficient solar-to-thermal energy storage. Adv Compos Hybrid Mater 8:400. https://doi.org/10.1007/s42114-025-01467-y
4. Liu W-W, Wang S-P, Li S-Z, Cao H, Feng C-P, Chen M, Bai L, Yang J, Yang W (2026) Integrated Design of Thermoconductive Mechanically Supporting Architectures for Manufacturing Ultra-Stretchable Thermally Conductive Composite Phase Change Materials. Adv Funct Mater 36:e75855. https://doi.org/https://doi.org/10.1002/adfm.75855
5. Shi J, Qin M, Aftab W, Zou R (2021) Flexible phase change materials for thermal energy storage. Energy Storage Mater 41:321–342. https://doi.org/https://doi.org/10.1016/j.ensm.2021.05.048
6. Wu S, Li T, Zhang Z-Y, Li T, Wang R (2021) Photoswitchable phase change materials for unconventional thermal energy storage and upgrade. Matter 4:3385–3399. https://doi.org/https://doi.org/10.1016/j.matt.2021.09.017
7. Gowthami D, Sharma RK (2023) Influence of Hydrophilic and Hydrophobic modification of the porous matrix on the thermal performance of form stable phase change materials: A review. Renew Sustain Energy Rev 185:113642. https://doi.org/https://doi.org/10.1016/j.rser.2023.113642
8. Wang H, Yan J, Lan X, Liu X (2025) In Situ Encapsulation of Co-N/C Nanocatalyst into Carbon Nanocubes for Selective Degradation of Sulfadiazine: High-Performance, Confinement Effect, and Bio-Toxicity Assessment. SusMat 5: e70042. https://doi.org/10.1002/sus2.70042

9. Chen Y, Zhou K, Du S (2025) Introducing carbon nanotubes into concrete: a porosity-based characterization of dispersion. Constr Build Mater 498:143947. https://doi.org/https://doi.org/10.1016/j.conbuildmat.2025.143947
10. Ateş A, Evgin B, Karaoğlu F (2026) Influence of Metal Oxide Incorporation on the Structure, Surface Features, and Hydrogen Storage Behavior of ZIF-8. ACS Omega 11:41732–41746. https://doi.org/10.1021/acsomega.6c01498
11. Kumari S, Katoch G, Somvanshi A, Lal B, Suman, Alsayari A, Wahab S, Kumari A, Kandwal A, Jasrotia R (2026) Metal-organic frameworks and their derivatives for electrocatalytic water splitting and hydrogen production: Progress, mechanisms, and perspectives. J Power Sources 689:240681. https://doi.org/https://doi.org/10.1016/j.jpowsour.2026.240681
12. Li Y, Liu P, Gao Y, Feng Y, Li P, Chen X (2024) Scattered Co-anchored MoS_2 synergistically boosting photothermal capture and storage of phase change materials. J Energy Chem 95:208–215. https://doi.org/10.1016/j.jechem.2024.03.024
13. Shahzadi S, Akhtar M, Arshad M, Ijaz MH, Janjua MRSA (2024) A review on synthesis of MOF-derived carbon composites: innovations in electrochemical, environmental and electrocatalytic technologies. RSC Adv 14:27575–27607. https://doi.org/10.1039/d4ra05183a
14. Furukawa S, Hirai K, Nakagawa K, Takashima Y, Matsuda R, Tsuruoka T, Kondo M, Haruki R, Tanaka D, Sakamoto H, Shimomura S, Sakata O, Kitagawa S (2009) Cover Picture: Heterogeneously Hybridized Porous Coordination Polymer Crystals: Fabrication of Heterometallic Core-Shell Single Crystals with an In-Plane Rotational Epitaxial Relationship. Angew Chem Int Ed 48:1697–1697. https://doi.org/https://doi.org/10.1002/anie.200990041
15. Choi S, Kim T, Ji H, Lee HJ, Oh M (2016) Isotropic and Anisotropic Growth of Metal-Organic Framework (MOF) on MOF: Logical Inference on MOF Structure Based on Growth Behavior and Morphological Feature. J Am Chem Soc 138:14434–14440. https://doi.org/10.1021/jacs.6b08821
16. Yin H, Huang M, Wang L, Muhammad S, Isimjan TT, Guo J, Cai D, Wang B, Yang X (2025) Lattice-mismatched MOF-on-MOF nanosheets with rich oxygen vacancies show fast oxygen evolution kinetics for large-current water splitting. Appl Catal B: Environ Energy 367:125105. https://doi.org/https://doi.org/10.1016/j.apcatb.2025.125105
17. Sun X, Pashkin A, Moebus F, Hübner R, Winnerl S, Helm M, Dimakis E (2024) Separated Electronic and Strain Interfaces in Core/Dual-Shell Nanowires: Unlocking the Potential of Strained GaAs for Applications Across Near-Infrared. Adv Funct Mater 34:2400883. https://doi.org/https://doi.org/10.1002/adfm.202400883
18. Guo R, Xu Y, Chen Y, Kuklin A, Zhang X, Cui D, Wang X, Ågren H, Huang H, Zhang Y (2026) Defect and Interface Co-Regulation Enabled Piezoelectricity Activation in $SnSe_2$ for High-Performance Piezo-Photocatalytic H_2O_2 Generation and Uranium Extraction. Adv Funct Mater 36:e76664. https://doi.org/https://doi.org/10.1002/adfm.76664
19. Dai J, Fan Z, Long Y, Yue W, Huang F, Jiao Y, Deng Y, Chang Y, Wang D (2024) Remarkably Boosting Piezocatalytic Performance of $Sr_{0.5}Ba_{0.5}Nb_2O_6$ Piezoceramics via Size Optimization and Oxygen

Vacancy Engineering. Adv Funct Mater 34:2408754. https://doi.org/https://doi.org/10.1002/adfm.202408754

20. Wen H, Zhang Z, Guo Y, Luo W, Si S, Yin T, Wu H, Huang S (2023) Synergistic Full-Scale Defect Passivation Enables High-Efficiency and Stable Perovskite Solar Cells. Adv Energy Mater 13:2301813. https://doi.org/https://doi.org/10.1002/aenm.202301813
21. Miao Y, Zhao Y, Zhang S, Shi R, Zhang T (2022) Strain Engineering: A Boosting Strategy for Photocatalysis. Adv Mater 34:2200868. https://doi.org/https://doi.org/10.1002/adma.202200868
22. Li X, Song J, Ma J, Wang J (2026) High-Entropy Electrocatalysts for Water Splitting: A Review on Structures, Synthesis, Scale-Up Challenges and Rational Designs. Adv Funct Mater 36:e22273. https://doi.org/https://doi.org/10.1002/adfm.202522273
23. Xie S, Liu W, Wan X, Lyu J, Yan F, Ouyang Y, Li X, Liu Y, Wang Z, Wang R, Wu J, Zhang Q, Tang X (2023) Rational Manipulation of Epitaxial Strains Enabled Valence Band Convergence and High Thermoelectric Performances in Mg3Sb2 Films. Adv Funct Mater 33:2300154. https://doi.org/https://doi.org/10.1002/adfm.202300154
24. Mansoor A, Jabar B, Li F, Jamil S, Fasehullah M, Chen Y-X, Liang G-X, Fan P, Zheng Z-H (2023) Strain-Mediated Lattice Rotation Design for Enhancing Thermoelectric Performance in Bi2S2Se. Adv Funct Mater 33:2302770. https://doi.org/https://doi.org/10.1002/adfm.202302770
25. Kim BC, Kim Y, Lee G-H (2026) Precision Local Strain Engineering in 2D Semiconductors and Their van der Waals Heterostructures. Small 22:e12902. https://doi.org/https://doi.org/10.1002/smll.202512902
26. Xu X, Liu H, Li D, Wang Q, Zhu X, Liu D, Chen X (2023) Lattice tensile strain cobalt phosphate with modulated hydroxide adsorption and structure transformation towards improved oxygen evolution reaction. J Colloid Interface Sci 650:498–505. https://doi.org/https://doi.org/10.1016/j.jcis.2023.07.006
27. Wang F, Zhou H, He Y, Zheng W (2026) Enhanced oxygen evolution of metastable LaFeCoNiMnMo high-entropy alloys produced by La-induced intense lattice distortion. Appl Surf Sci 736:166777. https://doi.org/https://doi.org/10.1016/j.apsusc.2026.166777
28. Liu Y, Hua X, Xiao C, Zhou T, Huang P, Guo Z, Pan B, Xie Y (2016) Heterogeneous Spin States in Ultrathin Nanosheets Induce Subtle Lattice Distortion To Trigger Efficient Hydrogen Evolution. J Am Chem Soc 138:5087–5092. https://doi.org/10.1021/jacs.6b00858
29. Liu Z, Shen J, Feng S, Huang Y, Wu D, Li F, Zhu Y, Gu M, Liu Q, Liu J, Zhu M (2021) Ultralow Volume Change of P2-Type Layered Oxide Cathode for Na-Ion Batteries with Controlled Phase Transition by Regulating Distribution of Na^+. Angew Chem Int Ed 60:20960–20969. https://doi.org/https://doi.org/10.1002/anie.202108109
30. Peng P, Geng Y, Nan J, Li S, Zhang D, Lin Q, Gong Y, Tang G (2026) High Thermoelectric Performance Achieved by Manipulating the Band Structure and Lattice Dislocations in n-Type Ge/Pb/Br Codoped Polycrystalline SnSe. Carbon Energy 8:e70217. https://doi.org/https://doi.org/10.1002/cey2.70217

31. Wu Y, Chen Z, Nan P, Xiong F, Lin S, Zhang X, Chen Y, Chen L, Ge B, Pei Y (2019) Lattice Strain Advances Thermoelectrics. Joule 3:1276–1288. https://doi.org/https://doi.org/10.1016/j.joule.2019.02.008
32. Koo Y, Kim Y, Choi SH, Lee H, Choi J, Lee DY, Kang M, Lee HS, Kim KK, Lee G, Park K-D (2021) Tip-Induced Nano-Engineering of Strain, Bandgap, and Exciton Funneling in 2D Semiconductors. Adv Mater 33:2008234. https://doi.org/https://doi.org/10.1002/adma.202008234
33. Zhen X, Wu H, Feng W, Chen H, Wang J, Chen H, Xu N, Shao L, Deng S-Z (2025) Single-Particle Plasmon Spectroscopy Revealing the Local Strain-Induced Band Structure Change in 2D Semiconductors. Adv Opt Mater 13:2500158. https://doi.org/https://doi.org/10.1002/adom.202500158
34. Kim E-B, Shaheer Akhtar M, Kong I, Ameen S (2025) Efficient environmental detection of heavy metal ions using porous Co-N/C rhombic dodecahedra from Zeolitic Imidazolate Frameworks (ZIF-67) via pyrolysis. J Water Process Eng 77:108509. https://doi.org/https://doi.org/10.1016/j.jwpe.2025.108509
35. Li Y-M, Liu Z-Y, Zhang Q-Y, Wang Y-J, Cui G-Q, Zhao Z, Xu C-M, Jiang G-Y (2023) Influence of carbonization temperature on cobalt-based nitrogen-doped carbon nanopolyhedra derived from ZIF-67 for nonoxidative propane dehydrogenation. Pet Sci 20:559–568. https://doi.org/https://doi.org/10.1016/j.petsci.2022.01.008
36. Jin X, Zhao X, Jin B, Tong L, Xu Z, Cao M, Liu G, Zhai J, Yang Z, Huang Q (2025) Integrated solid acid catalysis and photothermal conversion to regenerate CO_2-captured amine solutions using black TiO_2 nanoparticles. Chem Eng J 522:167295. https://doi.org/https://doi.org/10.1016/j.cej.2025.167295
37. Jiang Z, Song S, Zheng X, Liang X, Li Z, Gu H, Li Z, Wang Y, Liu S, Chen W, Wang D, Li Y (2022) Lattice Strain and Schottky Junction Dual Regulation Boosts Ultrafine Ruthenium Nanoparticles Anchored on a N-Modified Carbon Catalyst for H_2 Production. J Am Chem Soc 144:19619–19626. https://doi.org/10.1021/jacs.2c09613
38. Huang M, Zhou S-H, Yang C-J, Dong C-L, Jiao L, Ma D-D, Zhu Q-L, Huang Z (2026) Salt-Free Glycine Electrosynthesis via Carbon-Nitrogen Coupling Boosted by the Lattice Strain in Atomically Thin p-Block Bismuthene. ACS Nano 20:5135–5145. https://doi.org/10.1021/acsnano.5c19472
39. Elimian EA, Zhang M, Chen J, Jia H, Sun Y, He J (2022) Construction of Pt-mTiO_2/USY multifunctional catalyst enriched with oxygen vacancies for the enhanced light-driven photothermocatalytic degradation of toluene. Appl Catal B: Environ Energy 307:121203. https://doi.org/https://doi.org/10.1016/j.apcatb.2022.121203
40. Wang X-L, Fan H-L, Tian Z, He E-Y, Li Y, Shangguan J (2014) Adsorptive removal of sulfur compounds using IRMOF-3 at ambient temperature. Appl Surf Sci 289:107–113. https://doi.org/https://doi.org/10.1016/j.apsusc.2013.10.115
41. Ates M, Kuzgun O, Yildirim M, Ozkan H (2020) rGO/MnO_2/Polyterthiophene ternary composite: pore size control, electrochemical supercapacitor behavior and equivalent circuit model analysis. J Polym Res 27:202. https://doi.org/10.1007/s10965-020-02183-5

42. Hammerum S (2009) Alkyl Radicals as Hydrogen Bond Acceptors: Computational Evidence. J Am Chem Soc 131:8627–8635. https://doi.org/10.1021/ja901854t
43. Chen Y, Ding H, Gao J, Tang X, Liu Y, Yang M (2020) A novel strategy for enhancing the thermal conductivity of shape-stable phase change materials via carbon-based in situ reduction of metal ions. J Clean Prod 243:118627. https://doi.org/https://doi.org/10.1016/j.jclepro.2019.118627
44. Kim YB, Lee JJ, Lee J, Hong Y, Kwak S, Jung W (2026) Strain-Driven Surface Reconstruction During the Alkaline Oxygen Evolution Reaction: a Model Thin-Film Study. Adv Mater 38:e72847. https://doi.org/https://doi.org/10.1002/adma.72847
45. de Quilettes DW, Vorpahl SM, Stranks SD, Nagaoka H, Eperon GE, Ziffer ME, Snaith HJ, Ginger DS (2015) Impact of microstructure on local carrier lifetime in perovskite solar cells. Science 348:683–686. https://doi.org/10.1126/science.aaa5333
46. Wang Q, Cheng Q, Wang B, Zhang T, Liu Y, Zheng R, Chen S, Xing G, Qu S (2025) From Exciton Dynamics to Cell Fate: A Carbon Dot Based NIR Photocatalytic Platform for Pyroptosis via Self-Trapped Excitons. Adv Funct Mater 35:e10756. https://doi.org/https://doi.org/10.1002/adfm.202510756
47. Zhang M, Song Z, Wang Z, Wang A, Zhu G, Shao S (2021) Platinum quantum dots enhance electrocatalytic activity of bamboo-like nitrogen doped carbon nanotubes embedding Co-MnO nanoparticles for methanol/ethanol oxidation. J Colloid Interface Sci 590:164–174. https://doi.org/https://doi.org/10.1016/j.jcis.2021.01.045
48. Zheng F, Xia G, Yang Y, Chen Q (2015) MOF-derived ultrafine MnO nanocrystals embedded in a porous carbon matrix as high-performance anodes for lithium-ion batteries. Nanoscale 7:9637–9645. https://doi.org/10.1039/c5nr00528k
49. Zhao Y, Ren J, Liu Y, Tian Y, Xu D, Wang Z, Liu J, Wang Y, Gao R, Gong X (2026) Curvature-Activated Graphite Scaffolds Guide Charge Migration and Stress Distribution in Silicon Anodes. Adv Funct Mater 36:e27253. https://doi.org/https://doi.org/10.1002/adfm.202527253
50. Chen K, Li Y, Feng Y, Li X, Li Z, Liu S, Ge C, Chen X (2025) In situ vertical alignment of MoS_2 on Co/C dodecahedron boosting phase change materials for solar-thermoelectric generation. J Energy Chem 107:548–557. https://doi.org/https://doi.org/10.1016/j.jechem.2025.03.070
51. Wang K, Lu Z, Li Y, Wang S, Cao Y (2020) Interfacial Engineering of Bimetallic Carbide and Cobalt Encapsulated in Nitrogen-Doped Carbon Nanotubes for Electrocatalytic Oxygen Reduction. Chemsuschem 13:5539–5548. https://doi.org/https://doi.org/10.1002/cssc.202001619
52. Chen X, Lin J, Feng Y, Chen K, Qin M, Han S, Jiang Y, Shen Z, Li Y (2025) Carbon-metal network boosting photon/phonon transport in photothermal phase change materials. Carbon 238:120192. https://doi.org/https://doi.org/10.1016/j.carbon.2025.120192
53. Tang F, Wu X, Shen Y, Xiang Y, Wu X, Xiong L, Wu X (2022) The intercalation cathode materials of heterostructure MnS/MnO with dual ions defect embedded in N-doped carbon fibers for aqueous zinc ion batteries. Energy Storage Mater 52:180–188. https://doi.org/https://doi.org/10.1016/j.ensm.2022.07.033

54. Li Z, Lu J, Ding J, Hu Y, Wang W (2026) Interface-engineered CuS@NiCoSe with lattice strain: Synergizing photothermal conversion, gas adsorption, and stable catalysis for dry reforming of methane. J Colloid Interface Sci 704:139309. https://doi.org/https://doi.org/10.1016/j.jcis.2025.139309
55. Zheng JH, Jiang Q, Lian JS (2011) Synthesis and optical properties of flower-like ZnO nanorods by thermal evaporation method. Appl Surf Sci 257:5083–5087. https://doi.org/https://doi.org/10.1016/j.apsusc.2011.01.025
56. Han X-G, He H-Z, Kuang Q, Zhou X, Zhang X-H, Xu T, Xie Z-X, Zheng L-S (2008) Controlling Morphologies and Tuning the Related Properties of Nano/Microstructured ZnO Crystallites. J Phys Chem C 113:584–589. https://doi.org/10.1021/jp808233e
57. Sun Q, Yi Q, Luo H, Liu Q, Zhang D (2025) Improved piezo-photocatalytic activity by controlling the oxygen vacancy content of $NaNbO_3$ powders. J Alloys Compd 1010:177687. https://doi.org/https://doi.org/10.1016/j.jallcom.2024.177687
58. Zou H, Guo L, Xue H, Zhang Y, Shen X, Liu X, Wang P, He X, Dai G, Jiang P, Zheng H, Zhang B, Xu C, Wang ZL (2020) Quantifying and understanding the triboelectric series of inorganic non-metallic materials. Nat Commun 11:2093. https://doi.org/10.1038/s41467-020-15926-1
59. Lin Y, Zhu Y, Zhang B, Kim YA, Endo M, Su DS (2015) Boron-doped onion-like carbon with enriched substitutional boron: the relationship between electronic properties and catalytic performance. J Mater Chem A 3:21805–21814. https://doi.org/10.1039/c5ta03141a
60. Zhong W, Hong Q-L, Ai X, Zhang C, Li F-M, Li X-F, Chen Y (2024) RhNi Bimetallenes with Lattice-Compressed Rh Skin towards Ultrastable Acidic Nitrate Electroreduction. Adv Mater 36:2314351. https://doi.org/https://doi.org/10.1002/adma.202314351
61. Hao M, Qiu M, Yang H, Hu B, Wang X (2021) Recent advances on preparation and environmental applications of MOF-derived carbons in catalysis. Sci Total Environ 760:143333. https://doi.org/https://doi.org/10.1016/j.scitotenv.2020.143333
62. Yin C, Pan C-L, Pan Y, Hu J (2023) Hollow Mn-Co-O@C Yolk-Shell Microspheres with Carbon Shells as Cathodes Derived from a Double-Metal MOF for Aqueous Zinc-Ion Batteries. ACS Sustain Chem Eng 11:12397–12405. https://doi.org/10.1021/acssuschemeng.3c02847
63. Wang Y, Cai J, Wu M, Chen J, Zhao W, Tian Y, Ding T, Zhang J, Jiang Z, Li X (2018) Rational construction of oxygen vacancies onto tungsten trioxide to improve visible light photocatalytic water oxidation reaction. Appl Catal B: Environ Energy 239:398–407. https://doi.org/https://doi.org/10.1016/j.apcatb.2018.08.029
64. Lee BG, Hiller D, Luo J-W, Semonin OE, Beard MC, Zacharias M, Stradins P (2012) Strained Interface Defects in Silicon Nanocrystals. Adv Funct Mater 22:3223–3232. https://doi.org/https://doi.org/10.1002/adfm.201200572
65. Tang Z, Cheng P, Liu P, Gao Y, Chen X, Wang G (2023) Tightened 1D/3D carbon heterostructure infiltrating phase change materials for solar-thermoelectric energy harvesting: Faster and better. Carbon Energy 5:e281. https://doi.org/https://doi.org/10.1002/cey2.281

66. Liu Y, Li Z, Wang L, Yang X, Yang Y, Li X, Jiang Y, Gao Y, Lü W (2024) Surface Functional Modification for Boosting Power Density of Hydrovoltaic Devices. Adv Funct Mater 34:2312666. https://doi.org/https://doi.org/10.1002/adfm.202312666
67. Xiong J, Wang Y, Wang H, Xie L, Chai X, Zhang L, Peng W, Wang S, Du G, Xu K (2024) Electrospun biomass carbon-based porous nanofibers modified by green-dry cold plasma for gaseous formaldehyde adsorption. Ind Crops Prod 222:119769. https://doi.org/https://doi.org/10.1016/j.indcrop.2024.119769

Figures

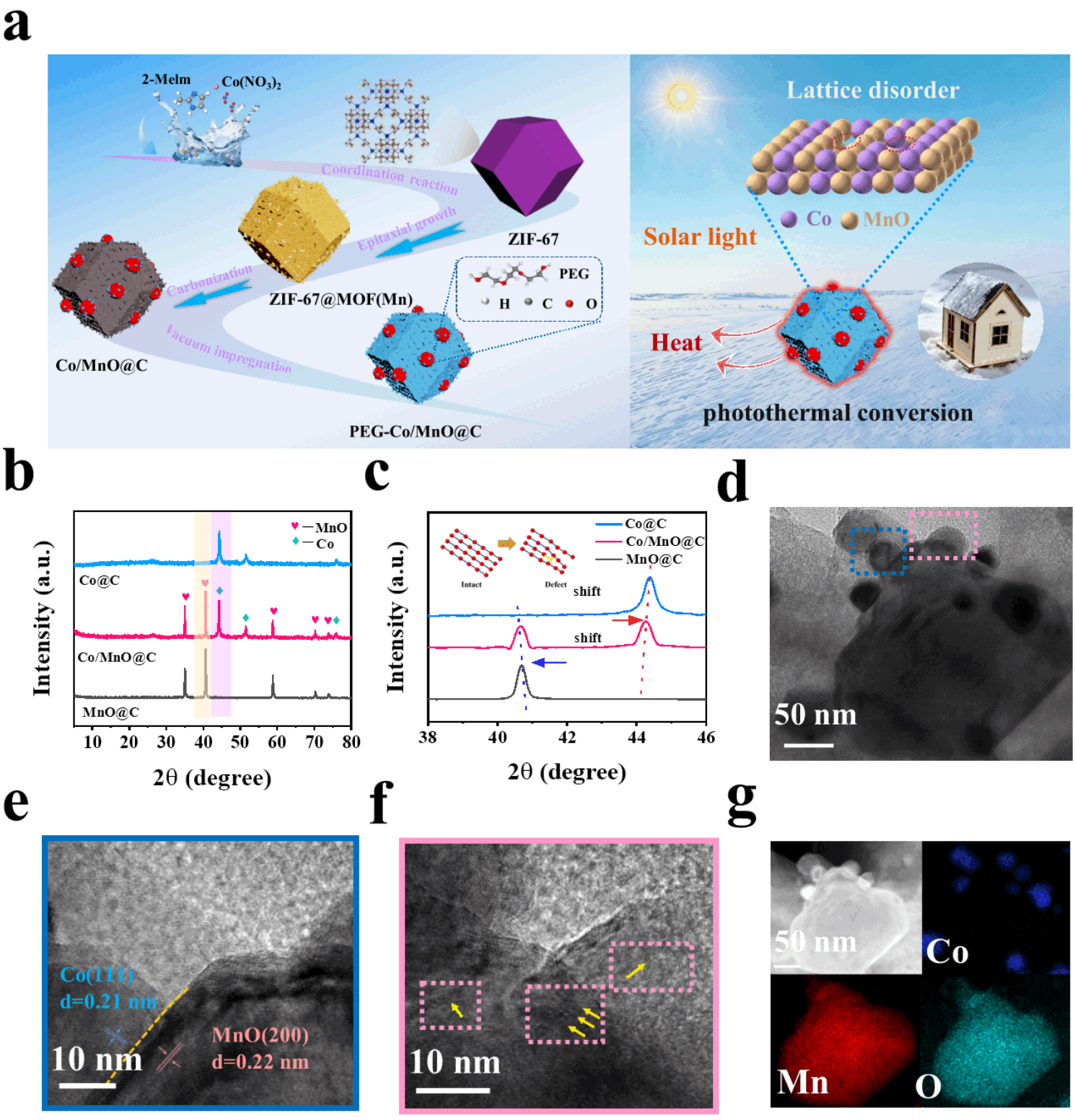


Figure 1

(a) Schematic diagram of the synthesis process of the Co/MnO@C. (b) XRD patterns of Co@C, MnO@C and Co/MnO@C. (c) Magnified XRD segment to display diffraction peak shift. (d) TEM image of Co/MnO@C. (e) HRTEM image of Co/MnO@C taken from the blue region in (d). (f) HRTEM images of Co/MnO@C taken from the pink region in (d). (g) HAADF image and corresponding EDS elemental mappings of Co/MnO@C.

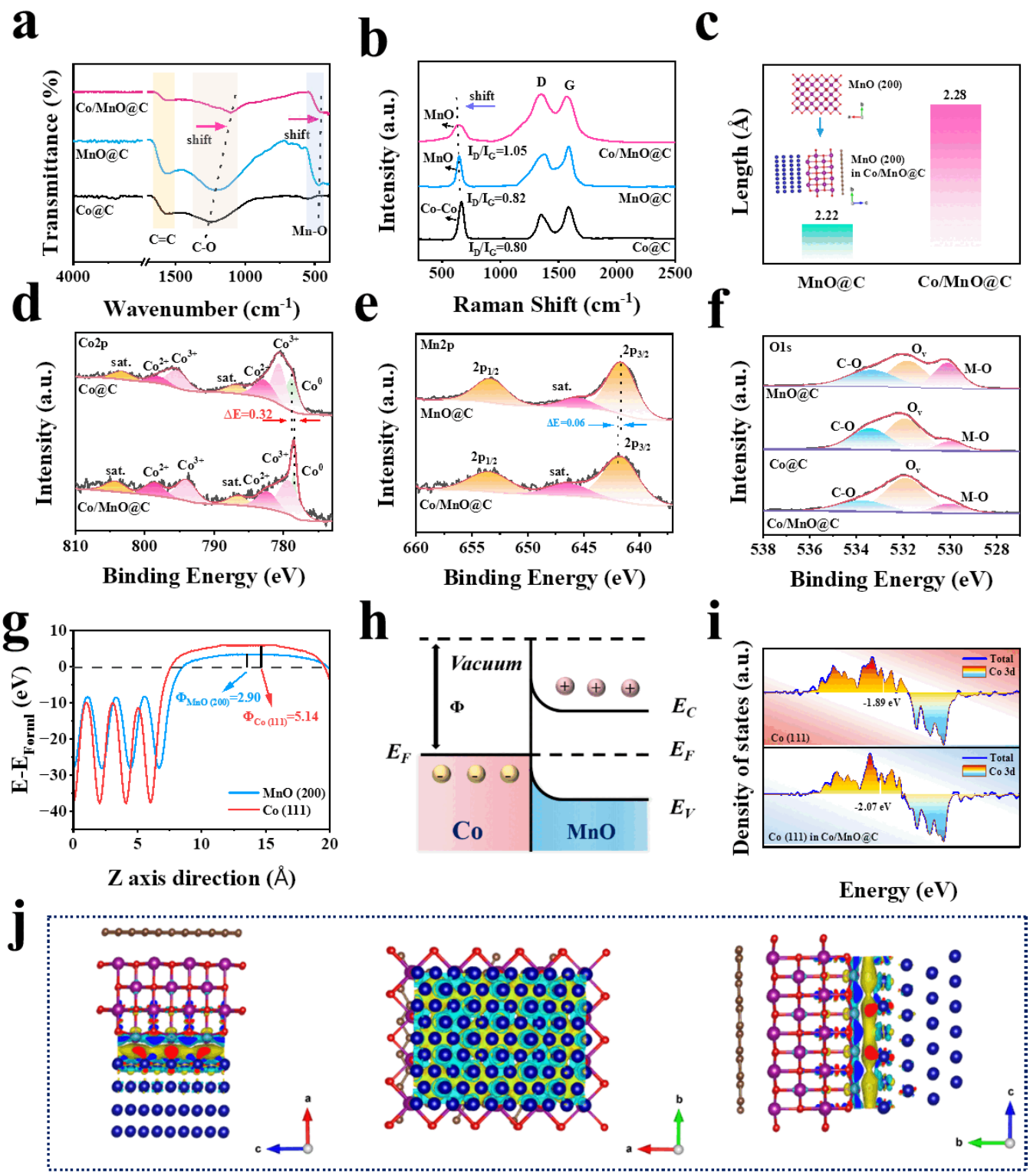


Figure 2

(a) FT-IR spectra and (b) Raman spectra of Co@C, MnO@C and Co/MnO@C. (c) DFT-calculated bond lengths of MnO (111) and MnO (111) in Co/MnO@C. Deconvoluted high-resolution XPS spectra: (d) Co 2p of Co@C and Co/MnO@C; (e) Mn 2p of MnO@C and Co/MnO@C; (f) O 1s of Co@C, MnO@C, and Co/MnO@C. (g) Calculated work function (φ) of MnO (200) and Co (111). (h) Schematic diagram of the

Mott-Schottky junction in the Co/MnO@C. (i) Calculated d-band center (εd) of the active Co sites. (j) Differential charge density diagrams of Co/MnO@C.

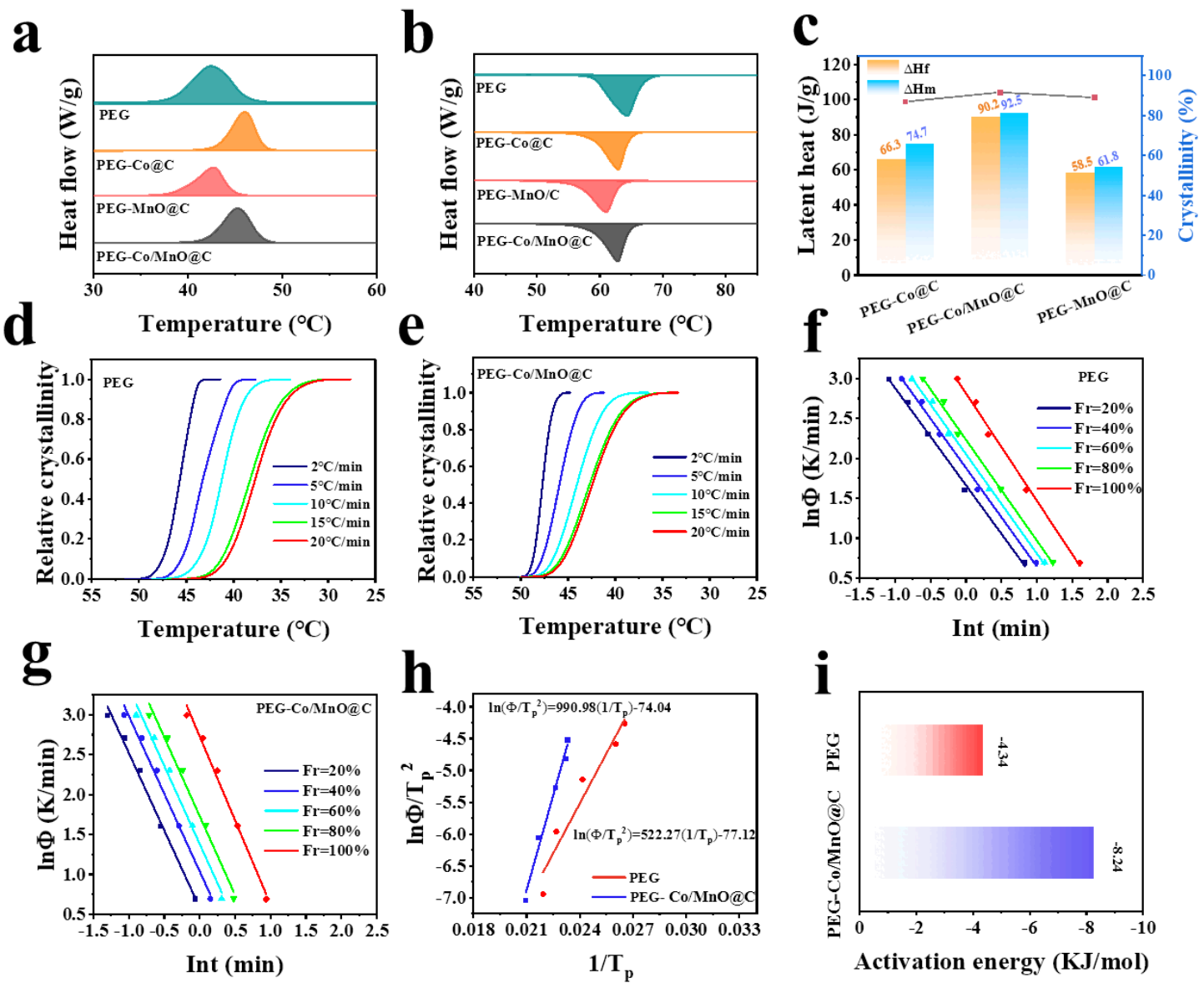


Figure 3

(a) Melting, (b) solidification DSC curves, and (c) corresponding enthalpies and crystallinities of different PCMs. (d) Fr-T diagrams of PEG. (e) Fr-T diagrams of PEG-Co/MnO@C. (f) lnΦ-Int curves of PEG. (g) lnΦ-Int curves of PEG-Co/MnO@C. (h) $\ln(\Phi/T_p^2)$ versus $1/T_p$ plots and (i) apparent activation energyof PEG and PEG-Co/MnO@C.

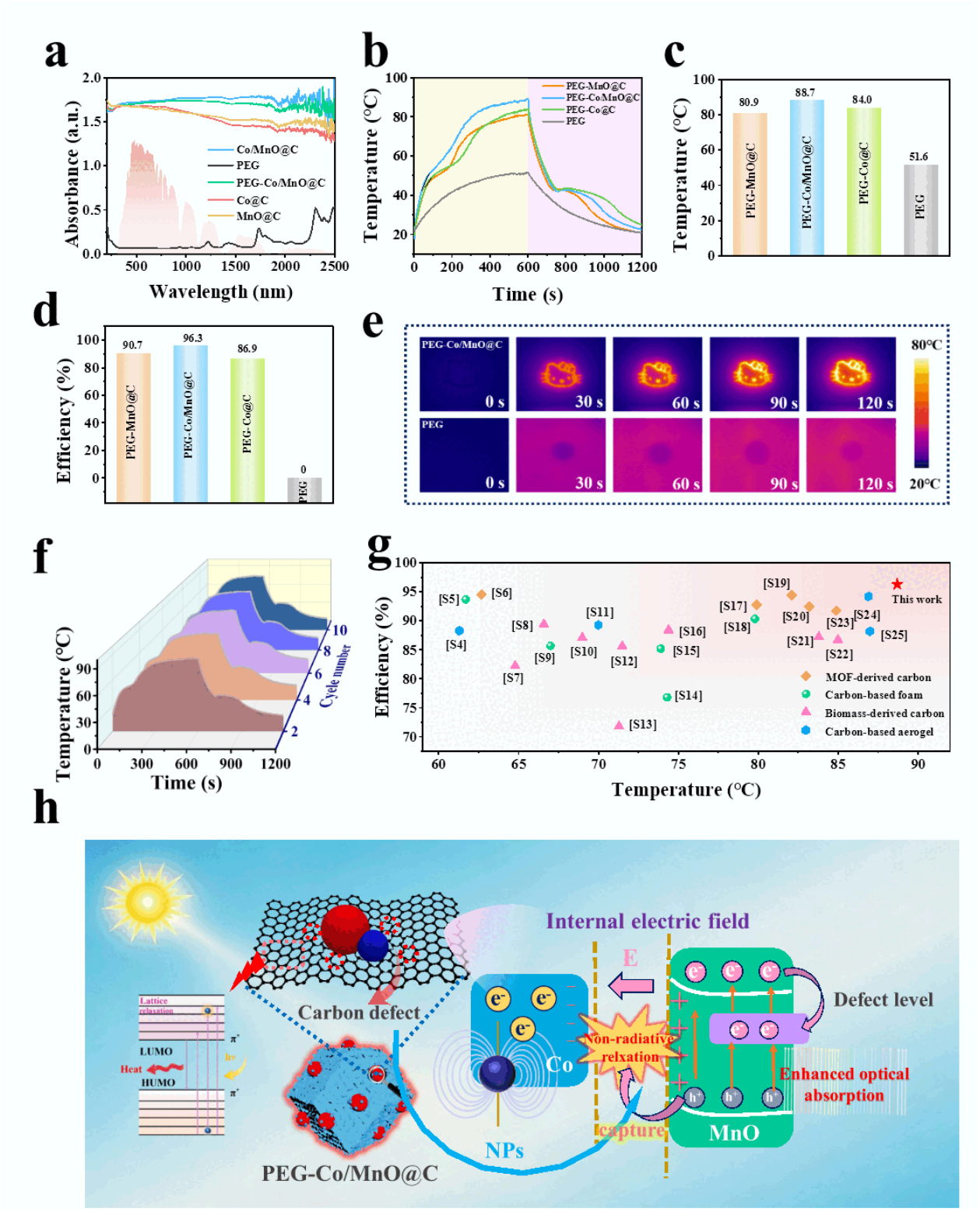


Figure 4

(a) UV-Vis-NIR absorption spectra of Co@C, MnO@C, Co/MnO@C, PEG-Co/MnO@C, PEG. (b) Time-temperature evolution curves, (c) saturation temperature and (d) corresponding photothermal storage efficiencies of PEG-Co@C, PEG-MnO@C, PEG-Co/MnO@C and PEG under solar simulator radiation at an intensity of 100 mW/cm^2. (e) Infrared thermal images of PEG and PEG-Co/MnO@C. (f) Time-temperature

evolution curves of PEG-Co/MnO@C during photothermal cycling. (g) Comparison of photothermal performance of PEG-Co/MnO@C with that of the composite PCMs reported in the literature.

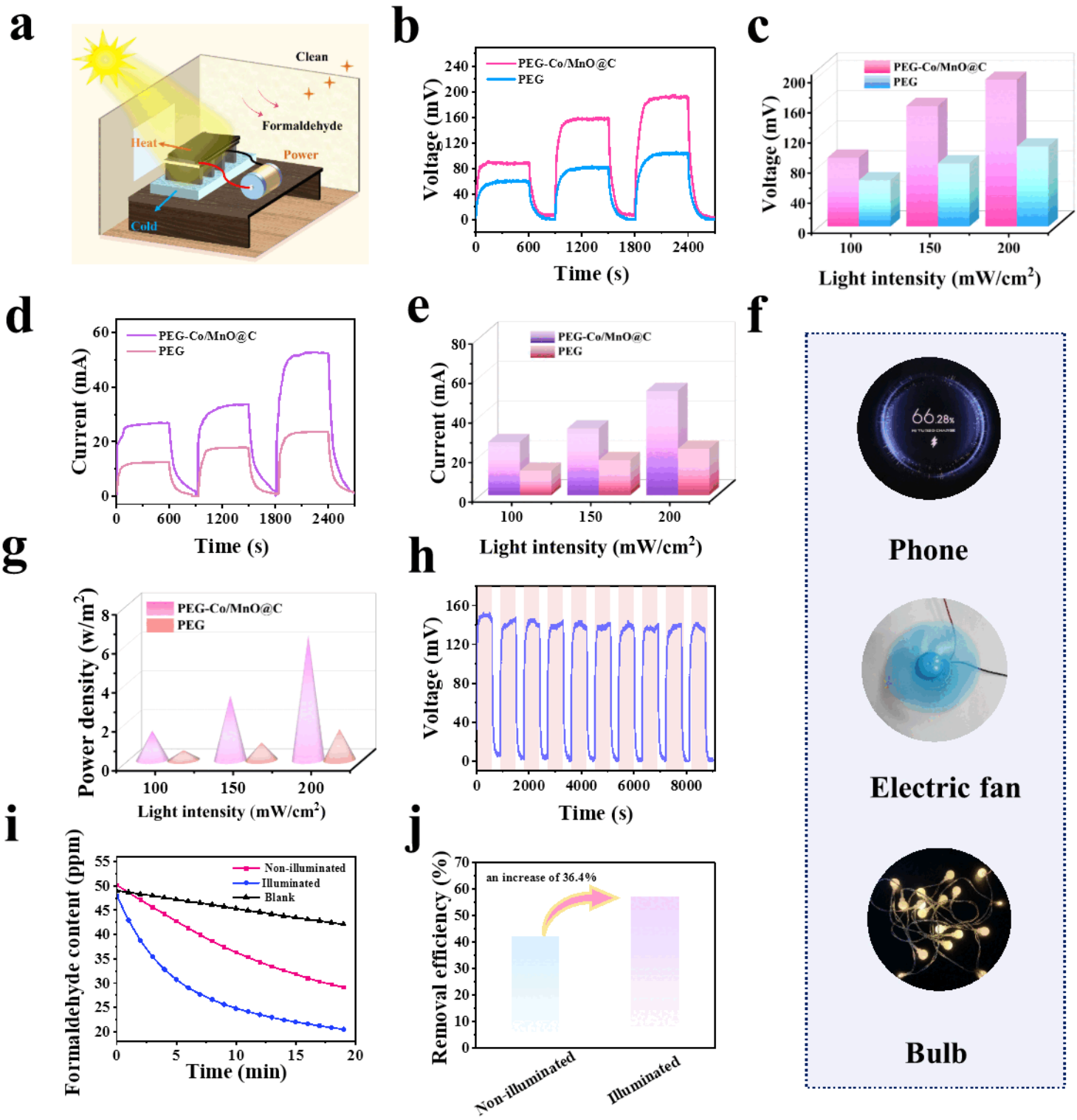


Figure 5

(a) Schematic diagram of PEG-Co/MnO@C for potential photo-thermal-electric generation and formaldehyde removal applications. (b) Output voltage and (c) corresponding data of PEG and PEG-Co/MnO@C under different solar radiation intensities. (d) Output current and (e) corresponding

data of PEG and PEG-Co/MnO@C under different solar radiation intensities. (f) Demonstration of the photo-thermal-electric conversion device directly powering electronic devices. (g) Calculated power density of PEG and PEG-Co/MnO@C. (h) Time-current curves of PEG-Co/MnO@C over ten cycles. (i) Formaldehyde removal diagram and (j) removal rates under light and dark conditions.

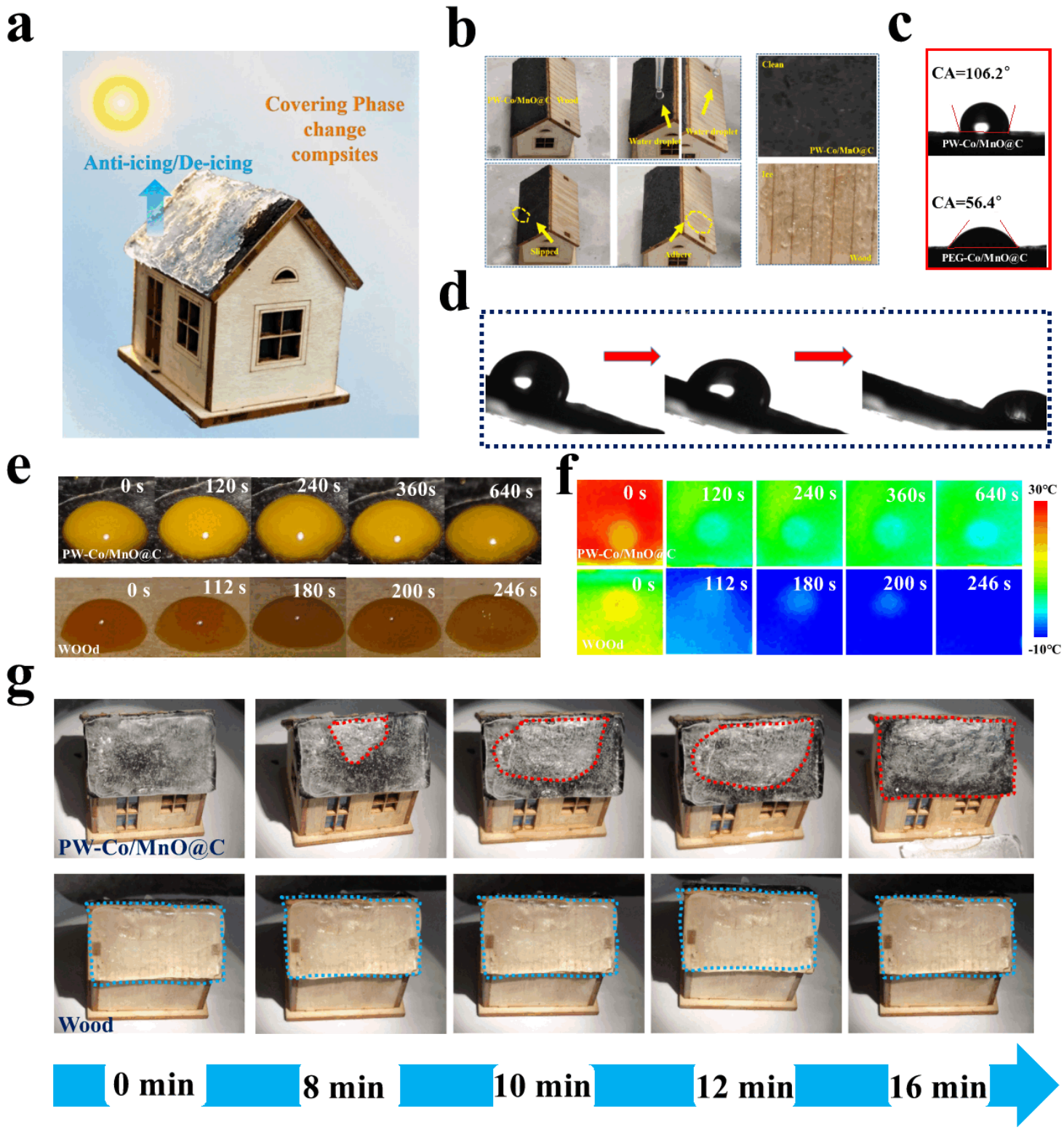


Figure 6

(a) Schematic diagram of anti-icing/deicing on a model house in a simulated low-temperature environment. (b) Efficient anti-icing of PW-Co/MnO@C. (c) Contact angles of PW-Co/MnO@C and PEG-Co/MnO@C. (d) Sliding characteristics of PW-Co/MnO@C on a 20° inclined surface. (e) Icing delay process of droplets on PW-Co/MnO@C and wood surfaces. (f) Infrared thermal images of delayed icing of droplets on PW-Co/MnO@C and wood surfaces. (g) Deicing performance of the PW-Co/MnO@C and the wood surface under solar irradiation at 100 mW/cm^2 (-20 ℃, ice film thickness of 4 mm).

Supplementary Files

This is a list of supplementary files associated with this preprint. Click to download.

- SI.docx